Dalton Transactions

ROYAL SOCIETY OF CHEMISTRY

PAPER

View Article Online
View Journal | View Issue

Cite this: *Dalton Trans.*, 2025, **54**, 12534

Immobilization of Keggin-type polyoxometalates in cyclodextrin-based polymers for oxidation catalysis†

Sana Aniba,[a,b] Nathalie Leclerc,[b] Clément Falaise,[b] Catherine Roch-Marchal,[b] Samah Akriche,[a] Emmanuel Cadot[b] and Mohamed Haouas *[b]

Immobilization of polyoxometalates (POMs) in organic materials by electrostatic attraction has emerged as one of the most effective methods to design robust and efficient heterogeneous catalysts. However, alternative strategies based on other weak supramolecular interactions, such as molecular recognition, remain less explored. In the present work, we investigate the adsorption capacity of insoluble γ-cyclodextrin (γ-CD)-based polymers towards Keggin-type POMs driven by the chaotropic effect, to design supramolecular hybrid composites for oxidative catalysis. First, the polymeric host materials were synthesized by crosslinking γ-CD with epichlorohydrin (EPI) and fully characterized by infrared spectroscopy, solid-state NMR and thermogravimetric analysis (TGA). Four POMs, $[PW_{12}O_{40}]^{3-}$, $[PV^{V}W_{11}O_{40}]^{4-}$, $[PV^{IV}W_{11}O_{40}]^{5-}$, and $[H_2W_{12}O_{40}]^{6-}$, with different ionic charges and chemical compositions, were studied to evaluate and compare their adsorption kinetics and equilibrium isotherms. The results show a fast and efficient adsorption process for all POMs, characterized by pseudo-second-order kinetics and a Langmuir isotherm model. The obtained POM@CD–EPI hybrids were then tested as heterogeneous catalysts in the oxidation reaction of benzyl alcohol. Excellent catalytic performances in terms of conversion (up to 100%), selectivity towards benzoic acid (up to 100%), and recyclability (up to 5 cycles) were achieved under mild conditions (60 °C/24 h) using *tert*-butyl hydroperoxide as the oxidizing agent. However, the use of H_2O_2 as an oxidant led to lower catalytic performance due to the rapid degradation of the POM–polymer composites under these conditions. It is then proposed that the POM–CD host–guest supramolecular arrangement plays a key role in both catalyst stability and the selective oxidation mechanism.

Received 4th June 2025,
Accepted 12th July 2025

DOI: 10.1039/d5dt01317h

rsc.li/dalton

Introduction

Polyoxometalates (POMs) represent a class of water-soluble ionocovalent oxides built from group V and VI transition metals of high oxidation states such as $V^{IV/V}$, $Mo^{V/VI}$ or $W^{V/VI}$.[1] Vanadium-containing mixed POMs are attracting attention because of their outstanding performance in homogeneous and heterogeneous oxidation catalysis for the conversion of organic substrates.[2–5] Keggin or Dawson-type vanadotungstate structures are generally obtained from an aqueous solution by selective addition of vanadium centers onto vacant POMs containing tetrahedral heteroatoms, such as P^{V}. The association of POMs with organic units has attracted growing interest in recent years for the added value these hybrids provide, notably the synergistic effects between organic and inorganic moieties in catalytic applications.[6–10]

Heterogeneous catalysis with POMs is preferred for practical reasons, in particular to facilitate catalyst recycling.[11] In the past few decades, many supports have been examined for the immobilization of POMs, *e.g.*, silica, ion-exchange resins, polymers, ionic liquids, and metal–organic frameworks (MOFs).[12–16] Encapsulation of POMs in various polymer materials, such as microgels, ionogels or biopolymers, can be achieved through various physicochemical processes to obtain responsive multifunctional materials with improved optical, mechanical or magnetic properties.[17–19] Incorporation of POM anions into these host matrices usually occurs *via* weak supramolecular interactions, such as hydrogen bonding, electrostatic attraction, and ion–dipole interactions supported by solvent effects.

POMs, particularly those with lower charge density, can form very stable host–guest complexes with organic macrocycles such as γ-cyclodextrin (γ-CD) *via* molecular recognition

[a]*Laboratory of Chemical Materials, Faculty of Sciences of Bizerte, Carthage University, 7021 Zarzouna, Tunisia*
[b]*Institut Lavoisier de Versailles, UMR 8180 CNRS, UVSQ, Université Paris-Saclay, Versailles, France. E-mail: mohamed.haouas@uvsq.fr*

† Electronic supplementary information (ESI) available. See DOI: https://doi.org/10.1039/d5dt01317h

processes.[20,21] Their supramolecular association with γ-CD dramatically improves their hydrolytic stability and significantly alters their properties such as solubility, redox behavior, or reactivity.[22–24] In particular, improved catalytic performances are expected from these hybrids in terms of structural robustness against severe reaction conditions, such as temperature, pH, or corrosive environment.[25] Native CDs have shown a remarkable ability to form MOF-type ordered extended networks with POMs, exhibiting an enhanced capacity for capturing ionic species, *e.g.*, lithium cations or polyiodides.[26,27] CDs can also form polymeric structures when combined with crosslinking agents owing to their numerous –OH groups. Such condensation processes lead to stable bonds with different crosslinking units, often resulting in polymers of various water solubility and molecular weight.[28] Among the most readily available CD crosslinkers are diisocyanates, active carbonyl compounds, and epichlorohydrin (EPI).[29] Immobilization of POMs in CD-based polymers has only recently been achieved with α- and β-type CDs using hexamethylene diisocyanate (HDI)[21,30] and diphenyl carbonate,[31] respectively. In these hybrids and other similar POM-containing biopolymers, the host–guest interaction often results from the interplay of several phenomena such as inclusion, hydrogen bonding, and the chaotropic effect as driving forces for the self-assembly process.[32–34]

Herein, this study aims to prepare guest–host POM–CD composites as heterogeneous catalysts for the oxidative reaction of organic substrates. EPI-crosslinked γ-CD polymers were first synthesized to serve as extended host matrices for the capture and immobilization of archetypal Keggin-type POMs (Fig. 1). Polymerization of this large macrocyclic CD to obtain water-insoluble materials in high yield was found to be less efficient with the HDI crosslinker than with the EPI crosslinker. Detailed adsorption kinetics and isotherm studies were then carried out to optimize composite synthesis. Finally, the catalytic performances of the resulting hybrid materials were evaluated in the benzyl alcohol (BnOH) oxidation reaction.

Results and discussion

CD–EPI polymer synthesis and characterization

The polymer synthesis procedure is described in the ESI.† Three CD–EPI(*X*) polymers were prepared by varying the molar ratio *X* = EPI/CD. The solid products CD–EPI(15) and CD–EPI(20) obtained with 15 and 20 equivalents of EPI were found to be water-soluble, while synthesis with a larger amount of EPI (25 equivalents) gave a CD–EPI(25) polymer that was insoluble in water. This is consistent with the general trend that insoluble polymers are favored for higher EPI/CD, although many other synthesis parameters can also be taken into account, such as temperature, reaction time and base strength.[35,36] The nature of the CD must also be considered, as their reactivity differs significantly depending on the size of the macrocycle. Most studies reported in the literature have focused on the use of β-CD, and very little data are available on EPI-based polymers coupled to γ-CD.

NMR spectroscopy is a technique of choice for characterizing CD–EPI polymers, as it can quantify the degree of co-condensation between the CD and EPI moieties, and hence the CD content.[37,38] For soluble polymers, liquid-state ^{1}H NMR is preferred, while ^{13}C MAS NMR is more useful for solid samples. The ^{1}H NMR spectra of the two soluble polymers, CD–EPI(15) and CD–EPI(20), are compared to the spectrum of the native γ-CD in Fig. S1 in the ESI.† The native γ-CD exhibits six magnetically different types of protons, denoted H*i*, where *i* = 1 to 6 (see Fig. 2), whereas soluble polymers are characterized by much broader signals and poorly resolved spectra. These broadenings result from a wider distribution of local chemical environments in long-chain molecules, as well as from a significant decrease in the rotational correlation times due to larger, slower-moving molecules. Because of the lack of resolution, the signals from the polyglycerol chains representing the 'EPI' moieties could not be observed and are superimposed on the H2–H6 signals from the CD. However, their presence can be easily detected by integrating the signals in the

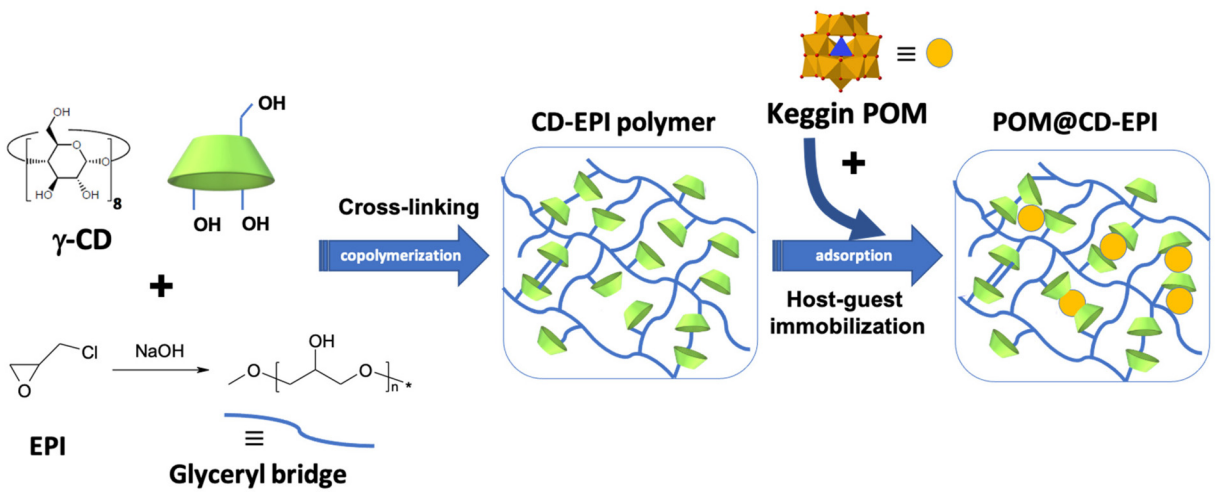

Fig. 1 Schematic representation of the immobilization of Keggin POM in a polymeric network of γ-CD copolymerized with epichlorohydrin.

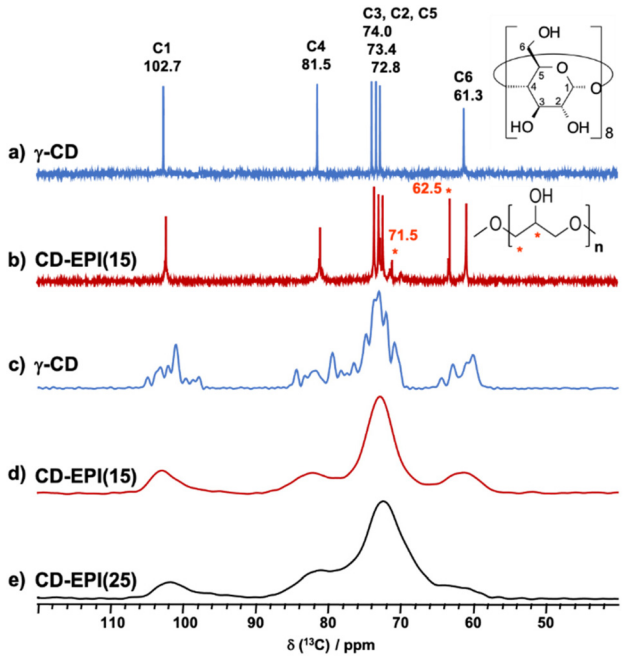

Fig. 2 $^{13}C\{^1H\}$ NMR spectra in (a and b) D_2O solution and at (c–e) the solid-state of the starting native γ-CD, the soluble CD–EPI(15), and the insoluble polymer CD–EPI(25).

range of 3.2–4.2 ppm against the H1 signal, which is not involved in any overlap (see the ESI† for details). The $^{13}C\{^1H\}$ NMR spectra of the soluble and insoluble polymers are shown in Fig. 2. The solution-state $^{13}C\{^1H\}$ NMR spectrum of the soluble polymer reveals that each carbon atom in the six-atom unit has a distinct electronic environment but undergoes some line broadening due to its inclusion within the polymeric matrix. We also note new features near signals C2 and C3 that could indicate that most of the condensation has occurred on the secondary rim of the macrocycle. Signals at *ca.* 62.5 ppm are observed and attributed to the glycerol functions due to EPI condensation. In the solid-state spectra, all resonances are broadened and partially or totally overlapped as those of polyglycerol moieties. The C1 carbon in the anomeric position is characterized by a deshielded signal at *ca.* 103 ppm and is therefore sufficiently resolved to be used to quantify the mass fraction of CD in the polymer (see Fig. S2 in the ESI† for details).

The chemical composition of the polymers can therefore be deduced from these quantitative NMR data, and the results are summarized in Table 1. The EPI/CD molar ratio in the polymer is always lower than the nominal amounts used in the synthesis, meaning that only a fraction of EPI per CD has reacted. The amount of CD in polymer materials remains relatively high, ranging from 50 to 80 wt%, which indicates that these materials are CD-rich. Increasing the amount of EPI in the synthesis medium produced an insoluble polymer, consistent with previous results,[36] probably favoring cross-linking with CD rather than self-polymerization into polyglycerol chains. Synthesis with a high amount of EPI should then favor multiple crosslinking with a single CD molecule. This may

Table 1 Polymer composition from quantitative NMR in solution and solid-state

Method	^{13}C MAS		^1H NMR in D_2O	
Sample	EPI/CD	CD wt%	EPI/CD	CD wt%
CD–EPI(15)[a]	7 ± 2	76 ± 4	6 ± 1	80 ± 8
CD–EPI(20)[a]	15 ± 2	60 ± 4	19 ± 2	55 ± 6
CD–EPI(25)[b]	21 ± 7	53 ± 9	—	—

[a] Water-soluble polymer. [b] Insoluble polymer.

explain why the EPI/CD ratio in the polymer is also steadily increasing linearly. These simultaneous reactions of several OH sites on a CD molecule promote rapid condensation and probably denser polymers. The comparison between solid-state ^{13}C NMR and solution-state ^1H NMR results for soluble polymers is remarkably consistent, validating the quantification methods, particularly by solid-state NMR for insoluble polymers.

Fourier Transform Infrared Spectroscopy (FTIR) is also a valuable tool to provide information on the functional groups present in the polymers.[39] In the IR spectra of the insoluble polymer and γ-CD (see Fig. S3†), common bands were observed such as the stretching vibrations of O–H, C–H, and C–C or C–O bonds at 3282, 2923, and 1073 cm^{-1}, respectively. Other bands can be observed at 1654 and 1429 cm^{-1}, corresponding to the bending deformation of H–O–H and C–O–H bonds, respectively. An absorption band at 2872 cm^{-1} is present in the spectrum of the CD–EPI polymer but absent in the spectrum of native CD, assigned to the CH/CH_2 group from the glycerol units.

The thermal stability of the insoluble polymer was studied by thermogravimetric analysis (TGA). A careful examination of the thermogravimetric curve, shown in Fig. S4,† reveals that intensive washing of the polymer with an acidic buffer solution (see the Experimental section in the ESI†) removed almost all the sodium trapped in the polymer during its synthesis ($R\text{-}ONa + H^+ \rightarrow R\text{-}OH + Na^+$). The washed insoluble polymer is stable up to 230 °C. Above this temperature, the sample begins to decompose in two stages of mass loss in the temperature range from 230 to 470 °C. The first loss, observed at 100 °C, corresponds to the release of water molecules (8% H_2O). The final thermal stage, in the temperature range from 230 to 470 °C, is attributed to the progressive degradation of the cyclodextrin-based polymeric structure.

Adsorption of POMs on CD–EPI polymers

Due to their multiple hydroxyl groups and ether linkages, water-insoluble CD–EPI composites swell when immersed, behaving like a hydrogel. This swelling could lead to the adsorption of POMs according to a process governed by the chaotropic effect taking place in solution where a large part of the polymer would be solvated. To verify this hypothesis, the ability of the synthesized insoluble polymer to adsorb POMs was tested and the optimum adsorption conditions for POM@CD–EPI composites were evaluated. All adsorption

experiments, including adsorption kinetics and isotherm studies, were carried out at room temperature (25 ± 1 °C), using 75 mg of polymer in 5 mL of POM solution at pH 1.0, under 500 rpm controlled stirring. The adsorption processes were monitored by UV-Vis spectroscopy for the colored POMs, $[PV^{IV}W_{11}O_{40}]^{5-}$ and $[PV^{V}W_{11}O_{40}]^{4-}$, and by TGA for colorless POMs $[PW_{12}O_{40}]^{3-}$ and $[H_2W_{12}O_{40}]^{6-}$.

The vanadium-substituted POM is yellow in its oxidized form $[PV^{V}W_{11}O_{40}]^{4-}$ and turns dark purple when reduced to one-electron $[PV^{VI}W_{11}O_{40}]^{5-}$. Initially, the CD–EPI parent polymer appears as a white powder and takes on the color of the POM upon adsorption, providing a qualitative indication of the efficiency of the adsorption process (Fig. S5†). The residual concentration of the POM in solution was monitored by UV-Vis spectroscopy (Fig. S6†), following the characteristic absorptions of the oxovanadium species observed at 424 nm (ε = 1680 L cm^{-1} mol^{-1}) for the oxidized species $[PV^{V}W_{11}O_{40}]^{4-}$ and at 510 nm (ε = 600 L cm^{-1} mol^{-1}) for the reduced derivative $[PV^{IV}W_{11}O_{40}]^{5-}$.[40,41]

Fig. 3a and b show the continuous decrease in UV-Vis absorbance of $[PV^{V}W_{11}O_{40}]^{4-}$ and $[PV^{IV}W_{11}O_{40}]^{5-}$ solutions as a function of contact time with the CD–EPI(25) polymer. The decrease in POM concentration in the solution reflects the adsorption process. Fig. 3c and d show the evolution of the adsorbed quantity q_t (μmol of POM per g of CD polymer) for the two POMs at different initial concentrations ranging from 0.05 to 3.2 mM (see section 1.3 in the ESI† for experimental details). It can be seen that increasing the concentration of POMs continuously increases the equilibrium adsorption quantities q_e for each concentration. This means that the adsorption capacity of the CD–EPI polymer towards these POMs is far from reaching its maximum limit compared to our experimental adsorption conditions (room temperature, pH 1). Furthermore, we find that for low concentrations, adsorption is very fast, reaching equilibrium after only 10 min and that for high concentrations, the equilibrium time increases, but only slightly. Again, this is a strong indication of the high capacity of the CD–EPI(25) polymer to adsorb these POMs. Nevertheless, overall, we observe a slightly higher adsorption capacity for $[PV^{V}W_{11}O_{40}]^{4-}$ than for $[PV^{IV}W_{11}O_{40}]^{5-}$ at a given concentration.

The adsorption kinetics were evaluated considering various kinetic models, *i.e.*, the pseudo-first-order model (PFOM), the pseudo-second-order model (PSOM), and the interparticle diffusion model (IDM). The best fits of experimental data were obtained with the PSOM presented in Fig. 3e and f when compared to the other two models shown in Fig. S7 and S8 in the ESI.† The plot of t/q_t *versus* time t showed almost perfect straight lines over the entire measurement range, and the main parameters of the calculated curves are reported in Table 2. The two POMs, $[PV^{V}W_{11}O_{40}]^{4-}$ and $[PV^{IV}W_{11}O_{40}]^{5-}$, behave similarly, indicating no apparent major effect of the oxidation state of the V center on the adsorption process.

The rapid decrease in adsorption rates with increasing POM concentration can be attributed to a drop in the number of available vacant sites due to the high affinity between the POM and the CD–EPI polymer. Indeed, the pseudo-second-order kinetics observed seem to indicate adsorption dominated by chemical factors.[41] POM molecules present in the adsorption medium can interact more readily with the interaction sites at lower concentrations, resulting in a higher rate constant. On the other hand, at higher concentrations, as saturation approaches, the rate constants of POM adsorption to

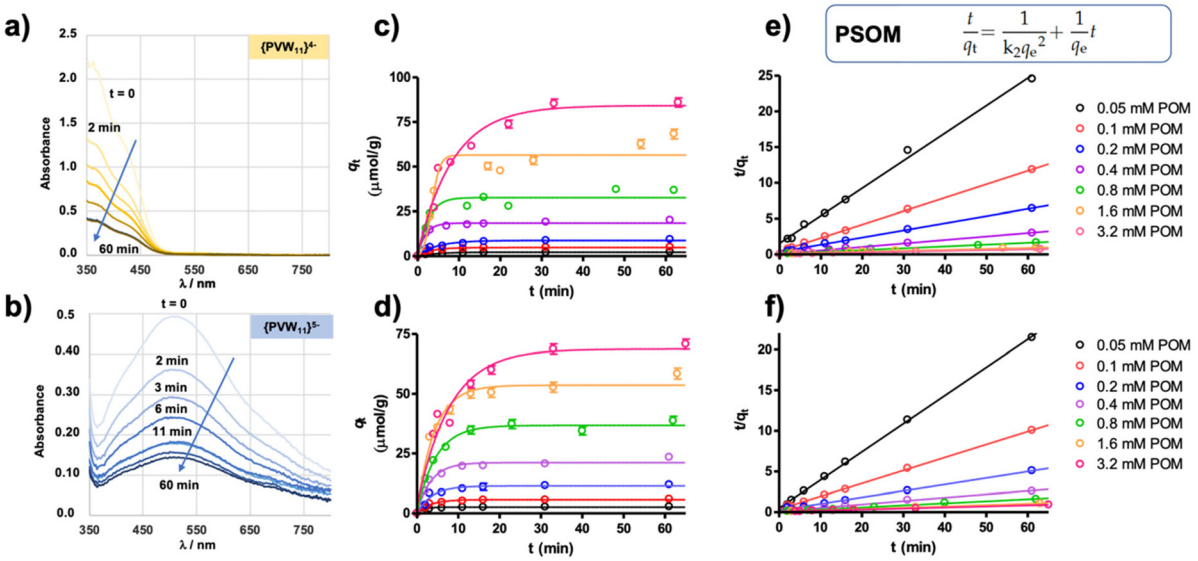

Fig. 3 (a and b) Evolution of the adsorption spectra of $[PV^{V}W_{11}O_{40}]^{4-}$ and $[PV^{IV}W_{11}O_{40}]^{5-}$ solution (0.8 mM) as a function of contact time with the insoluble polymer CD–EPI(25). (c and d) Plots of adsorbed quantity q_t (μmol g^{-1}) of $[PV^{V}W_{11}O_{40}]^{4-}$ and $[PV^{IV}W_{11}O_{40}]^{5-}$ as a function of contact time t for different POM concentrations, and (e and f) their corresponding pseudo-second-order model (PSOM) kinetic curves. Experimental conditions: CD polymer amount = 75 mg, POM volume = 5 mL, POM concentration = 0.05–3.2 mM, contact time = 0–60 min, stirring speed = 500 rpm, pH = 1, and temperature = 25 °C.

Table 2 PSOM kinetic parameters of adsorption of $PV^{V}W_{11}O_{40}^{4-}$ and $PV^{IV}W_{11}VO_{40}^{5-}$ on the CD–EPI(25) polymer

C_0 (mM)	K_2 (g μmol^{-1} min^{-1})	q_e calc (μmol g^{-1})	q_e exp[a] (μmol g^{-1})	R^2
		$PV^{V}W_{11}VO_{40}^{4-}$		
0.0457	0.10 ± 0.02	2.56 ± 0.07	2.5	0.9957
0.0984	0.084 ± 0.007	5.32 ± 0.03	5.1	0.9998
0.176	0.028 ± 0.004	10.0 ± 0.1	9.5	0.9991
0.356	0.030 ± 0.004	20.6 ± 0.2	20.2	0.9995
0.713	0.007 ± 0.003	38 ± 1	39	0.9895
1.43	0.0019 ± 0.0006	73 ± 4	68	0.9870
2.84	0.0015 ± 0.0003	97 ± 4	86	0.9913
		$PV^{IV}W_{11}VO_{40}^{5-}$		
0.0500	0.240 ± 0.04	2.89 ± 0.03	2.8	0.9996
0.104	0.07 ± 0.01	6.29 ± 0.08	6.06	0.9991
0.205	0.029 ± 0.008	12.5 ± 0.3	11.9	0.9971
0.435	0.013 ± 0.004	24 ± 1	23	0.9973
0.819	0.008 ± 0.002	40 ± 1	39	0.9948
1.69	0.0049 ± 0.0009	61 ± 1	58	0.9984
3.19	0.0024 ± 0.0005	78 ± 2	71	0.9958

[a] Value of the last point in the kinetic experiment (*i.e.*, contact time 60 min).

the polymer drop due to increased competition for the remaining adsorption sites. These observations confirm that chemical forces, *e.g.*, chemisorption, are the main causes of POM adsorption here, as opposed to physical forces, *e.g.*, diffusion.[42,43] Adsorption therefore takes place on specific active sites, probably the central cavity of the CD moiety to form inclusion complexes through hydrogen bonding or other driving forces related to the solvent effect. These results are consistent with the assertion that the rate constant of the pseudo-second-order model is a complex function of the initial solute concentration.[31]

Comparison between the results of the two POMs shows comparable orders of magnitude in adsorption rates, although adsorption is slightly faster with $[PV^{V}W_{11}O_{40}]^{5-}$ than with $[PV^{IV}W_{11}O_{40}]^{4-}$ at high concentrations. However, the equilibrium adsorption quantity q_e was found to be slightly higher with $[PV^{V}W_{11}O_{40}]^{4-}$ than with $[PV^{IV}W_{11}O_{40}]^{5-}$ at high concentrations (see Table 2). This observation is consistent with the fact that a high POM loading decreases the adsorption rate, as previously observed. Also, the overall trend showed a slightly better adsorption performance with the less charged POM, as might be anticipated from the chaotropic effect.[19]

To evaluate the POM release capacity of the POM@CD–EPI composites, the samples obtained with 1.6 mM POM were treated in a pH 1 sulfate buffer solution under 500 rpm stirring for 1 h at 25 and 60 °C. UV-Vis (Fig. S9†) measurements of the supernatants revealed a POM loading loss of only 1.5% and 8% for $[PV^{V}W_{11}O_{40}]^{4-}$, and 7% and 29% for $[PV^{IV}W_{11}O_{40}]^{5-}$ at RT and 60 °C, respectively. However, in the case of $[PV^{V}W_{11}O_{40}]^{4-}$, we noticed the reduction of the POM after its release at 60 °C, with the appearance of an absorption band at 510 nm. This is probably due to the oxidation of a few OH groups on the CDs by the POM. These results confirm that the adsorption is very strong, mainly chemisorption, and that physisorbed POMs, if any, are negligible.

Two other Keggin POMs, $[PW_{12}O_{40}]^{3-}$ and $[H_2W_{12}O_{40}]^{6-}$, carrying different negative charges were also studied for comparison. Adsorption equilibrium is reached when the quantity of POM adsorbed no longer changes over time. At this point, the amount of adsorbed POM inside the polymer is in dynamic equilibrium with the amount of POM desorbed. This equilibrium is reached after 1 h of contact, as previously observed with the other POMs. The adsorption is quantitatively evaluated by TGA, and Fig. 4 presents the results obtained. We note a difference in the thermal decomposition behavior: while with $[PW_{12}O_{40}]$@CD-EPI, the weight loss takes place in three stages and up to 650 °C, with $[H_2W_{12}O_{40}]$@CD–

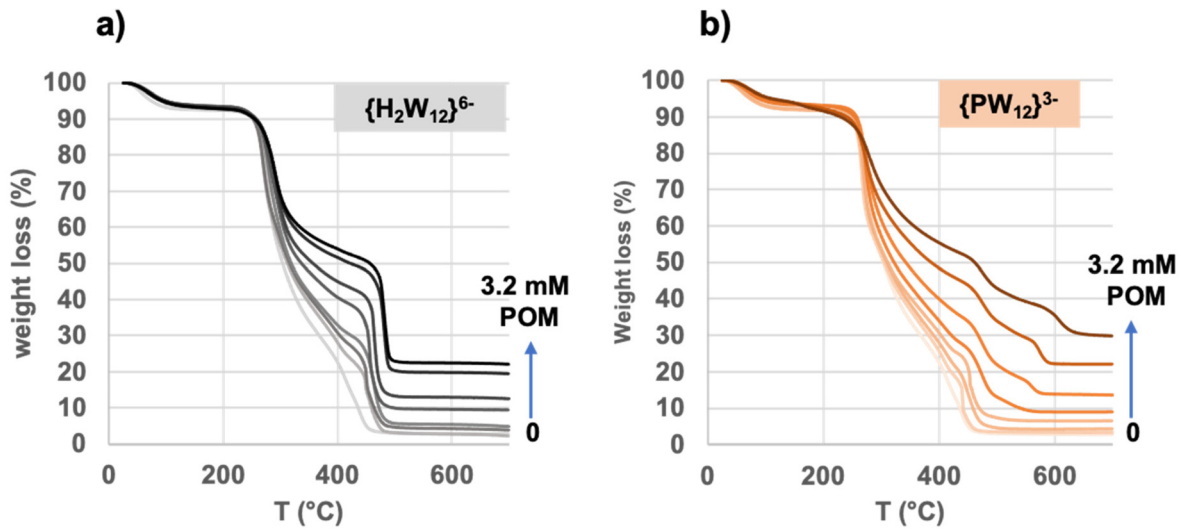

Fig. 4 TGA curves of POM@CD–EPI composites obtained upon adsorption of 5 mL of (a) $[H_2W_{12}O_{40}]^{6-}$ or (b) $[PW_{12}O_{40}]^{3-}$ solutions of varied concentrations on 75 mg of insoluble polymer CD–EPI(25). Experimental conditions: CD polymer amount = 75 mg, POM volume = 5 mL, POM concentration = 0–3.2 mM, contact time = 60 min, stirring speed = 500 rpm, pH = 1, and temperature = 25 °C.

EPI, the process is complete at a lower temperature (500 °C) involving only two steps. This may reflect a difference in the thermal stability of the POMs, which is higher for $[PW_{12}O_{40}]^{3-}$ than for $[H_2W_{12}O_{40}]^{6-}$. The solid residue obtained at 700 °C corresponds to the elemental oxides which result from the thermal decomposition of the POM, *e.g.*, WO_3, Na_2O, Rb_2O, or P_2O_5. Here, we calculate the quantity of POM adsorbed in the solid, and we then deduce by subtraction the quantity q_e resulting from the heterogeneous equilibrium between the solid and the solution.

To better understand the adsorption equilibrium, the adsorption isotherms are analyzed with the Langmuir model (see section 1.3 in the ESI†). The calculated curves are shown in Fig. 5. The parameters extracted from fitting of the experimental data are collected in Table 3. Extrapolation of the calculated models allowed for the estimation of maximum adsorption capacity q_{max}. The highest value of 135 μmolg^{-1} was found for $[PW_{12}O_{40}]^{3-}$, well above the values obtained for $[PV^{IV}W_{11}O_{40}]^{5-}$ and $[H_2W_{12}O_{40}]^{6-}$ in the 75–90 μmol g^{-1} range. This observation is in line with the general trend that follows the negative charge of POMs, *i.e.*, the lower the charge, the higher the adsorption capacity. The affinity for complexation at the molecular level between the γ-CD and Keggin-type POMs in aqueous solution is known to be mainly governed by the chaotropic character of the POM, which directly depends on the charge density of the nanoion.[17,20] These values also indicate that the POM/CD molar ratio decreases from 0.33, to 0.25, to *ca.* 0.2 when increasing the charge from 3−, to 4−, to −5/6, clearly showing that only a small fraction of CD is accessible to the POM. Both thermodynamic and R_L values indicate a favorable and spontaneous adsorption process. The R_L parameter varying from 0 to 1 across the studied POM concentration range, 0.05–3.2 mM, is consistent with favorable adsorption.[39,44] Consequently, the $\Delta G°$ associated with the adsorption process is negative, and falls in all cases in common values between −27 and −26 kJ mol^{-1}. These results demonstrate comparable strong affinity of the CD–EPI polymer towards Keggin POMs.

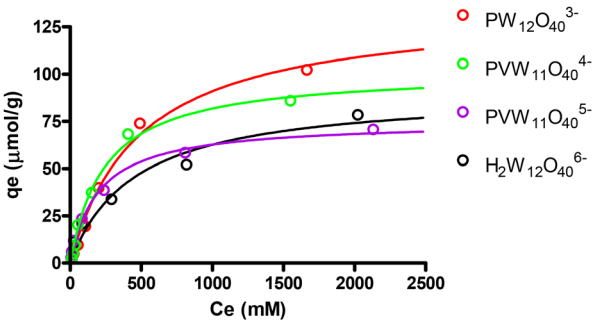

Fig. 5 Langmuir isotherm curves for the adsorption of $[PW_{12}O_{40}]^{3-}$, $[PV^{V}W_{11}O_{40}]^{4-}$, $[PV^{IV}W_{11}O_{40}]^{5-}$, and $[H_2W_{12}O_{40}]^{6-}$ on insoluble polymer CD–EPI(25). Experimental conditions: CD polymer amount = 75 mg, POM volume = 5 mL, POM concentration = 0–3.2 mM, contact time = 60 min, stirring speed = 500 rpm, pH = 1, and temperature = 25 °C.

Characterization of POM@CD–EPI composites

The final composites obtained by adsorption of a 3.2 mM POM solution onto the insoluble CD–EPI(25) polymer were subjected to further characterization by various techniques, including TGA, elemental analysis, FT-IR, and solid-state NMR spectroscopy. The main objective of these analyses is to identify and verify the chemical structure and composition of the POM and its interaction with its local environment.

The TGA of $[PVW_{11}O_{40}]^{4-/5-}$@CD–EPI composites (Fig. S10 and S11†) showed a final plateau with a difference of 17 and 21 wt% with respect to the plateau of the parent polymer, corresponding to POM residues of $[PV^{IV}W_{11}O_{40}]^{5-}$ and $[PV^{V}W_{11}O_{40}]^{4-}$, respectively. These amounts correspond to 70 and 91 μmol POM per 1 g of polymer, in perfect agreement with the values obtained by UV-Vis spectroscopy of 71 and 86 μmol g^{-1} observed with $[PV^{IV}W_{11}O_{40}]^{5-}$ and $[PV^{V}W_{11}O_{40}]^{4-}$, respectively. Quantitative elemental analyses were carried out to calculate the amount of POM adsorbed in the polymer (Tables S1 and S2†). ICP analyses tend to underestimate the P and V contents, while EDS measurement overestimates the P content. However, the observed P/V and W/V molar ratios of 1 and 11, respectively, match the expected values for an intact POM structure. The amounts of cations (Na and K) in the composites were found to be too low (*ca.* 30 μmol g^{-1}) to compensate for the negative charge of the POM. This content is very similar to that initially present in the parent polymer CD–EPI (25), indicating that the adsorbed POMs are rather in their protonic forms, *i.e.*, heteropolyacids. Thus, the chemical formula of the inorganic part in the composites based on ICP analyses

Table 3 Adsorption isotherm parameters from fitting curves of Fig. 5 [a] with the Langmuir model $\left(q_e = \frac{\frac{K_L}{a_L} C_e}{\frac{1}{a_L} + C_e}\right)$, and deduced maximum POM_{max}/CD capacity in the CD–EPI(25) composite

POM	K_L (L g^{-1})	q_{max} [b] (μmol g^{-1})	a_L (L μmol^{-1})	$\Delta G°$ [c] (kJ mol^{-1})	R_L [d]	POM_{max} per CD[e]
$[PW_{12}O_{40}]^{3-}$	0.28 ± 0.03	135 ± 9	0.0020 ± 0.0003	−26.5 ± 0.2	0.113–0.907	0.33
$[PV^{V}W_{11}O_{40}]^{4-}$	0.43 ± 0.04	102 ± 4	0.0042 ± 0.0005	−27.4 ± 0.2	0.078–0.840	0.25
$[PV^{IV}W_{11}O_{40}]^{5-}$	0.38 ± 0.04	75 ± 3	0.0050 ± 0.0008	−27.1 ± 0.3	0.059–0.800	0.18
$[H_2W_{12}O_{40}]^{6-}$	0.23 ± 0.03	90 ± 10	0.0025 ± 0.0006	−26.0 ± 0.3	0.111–0.889	0.22

[a] Determination coefficient R^2 in the range of 0.97–0.99. [b] $q_{max} = K_L/a_L$. [c] $\Delta G° = -RT\ln(Mw_{POM}C_{H_2O}K_L)$. [d] $R_L = 1/(1 + a_L C_0)$ for POM concentration range C_0 0.05–3.2 mM. [e] Calculated from q_{max} and 53 wt% CD (see Table 1).

is $Na_xH_{n-x}[PVW_{11}O_{40}]$, with x = 0.4–0.5 and n = 4 or 5 (for both reduced and oxidized POMs).

The functional groups of the polymer that are responsible for interactions with the POMs could be determined by FT-IR. Fig. S3† shows the FT-IR spectra of the POM@polymer composites compared to that of the POM used $K_5[PV^{IV}W_{11}O_{40}]\cdot16H_2O$, $K_4[PV^{V}W_{11}O_{40}]\cdot9H_2O$, the parent polymer CD–EPI(25), and the native γ-CD. The absorption band at 2870 cm^{-1}, corresponding to the vibrations of the new carbon skeleton linked to the cyclodextrin rings after copolymerization with epichlorohydrin,[39] is present in all composite materials. Characteristic POM bands at 960 and 880 cm^{-1}, attributed to W=O stretching and vibrational frequency of W–O_b–W (O_b = corner-sharing O),[45] respectively, are observed in all composite samples. In addition, we observe a slight shift in W–O_c–W vibrations (O_c = edge-sharing O), from 760 to 800 cm^{-1}, which could be attributed to an inclusion effect of the POM in the polymer. Similar high-frequency shifts have been observed when POMs are incorporated into mesoporous MOFs.[46,47]

Further analyses were carried out using solid-state NMR, as shown in Fig. 6. The ^{31}P MAS NMR spectra of the POM@CD–EPI composites are compared with the spectra of the corresponding original POM compounds, $K_5[PV^{IV}W_{11}O_{40}]\cdot16H_2O$ and $K_4[PV^{V}W_{11}O_{40}]\cdot9H_2O$, in Fig. 6a. The ^{31}P NMR spectrum of the $[PV^{IV}W_{11}O_{40}]^{5-}$ species shows a very broad signal as a result of the paramagnetic nature of the V^{IV} centers, while that of the diamagnetic $[PV^{V}W_{11}O_{40}]^{4-}$ contains a very narrow signal due to its highly symmetrical environment in the central cavity of the Keggin structure. The similarity of the spectra of the composites with those of their starting POM counterparts indicates the successful adsorption of the POM into the polymer without degradation or redox change of the initial POM. ^{51}V NMR is only possible for the diamagnetic POM $[PV^{V}W_{11}O_{40}]^{4-}$. The ^{51}V MAS spectra of $K_4[PV^{V}W_{11}O_{40}]\cdot9H_2O$ and $[PV^{V}W_{11}O_{40}]^{4-}$@CD–EPI shown in Fig. 6b are dominated by strong chemical shift anisotropy (CSA), while the quadrupolar coupling constants are moderate, of the order of 1 MHz.[48] Spectra recorded at various MAS rates were simulated using the DMfit program[49] to extract isotropic and anisotropic chemical shift parameters, δ_{iso}, Δ_{CSA}, and η_{CSA} (Fig. S13 and S14†). For the POM compound $K_4[PV^{V}W_{11}O_{40}]\cdot9H_2O$, the spectrum shows a composite signal consisting of a main resonance with a small shoulder. The dominant resonance has an isotropic chemical shift δ_{iso} of −565.4 ± 0.3 ppm, an axial tensor Δ_{CSA} of −153 ± 4 kHz, an asymmetry parameter η_{CSA} of 0.77 ± 0.06, and a full width at half-maximum (fwhm) of 1.0 kHz. The single resonance with its MAS sidebands observed in the composite $[PV^{V}W_{11}O_{40}]^{4-}$@CD–EPI is characterized by slightly different parameters, *i.e.*, δ_{iso} = −553.8 ± 0.3 ppm, Δ_{CSA} = −80 ± 10 kHz, η_{CSA} = 0.7 ± 0.1, and fwhm = 2.1 kHz. It is particularly interesting to note that the significant line broadening and the lower anisotropy of the chemical shift should indicate greater disorder and dispersion at the molecular level of the POM units in the polymer matrix. This comparison clearly shows that there is a wider distribution in the local chemical environment and more structural disorder around the POM in the $[PV^{V}W_{11}O_{40}]^{4-}$@CD–EPI composite than in the ionic salt $K_4[PV^{V}W_{11}O_{40}]\cdot9H_2O$.

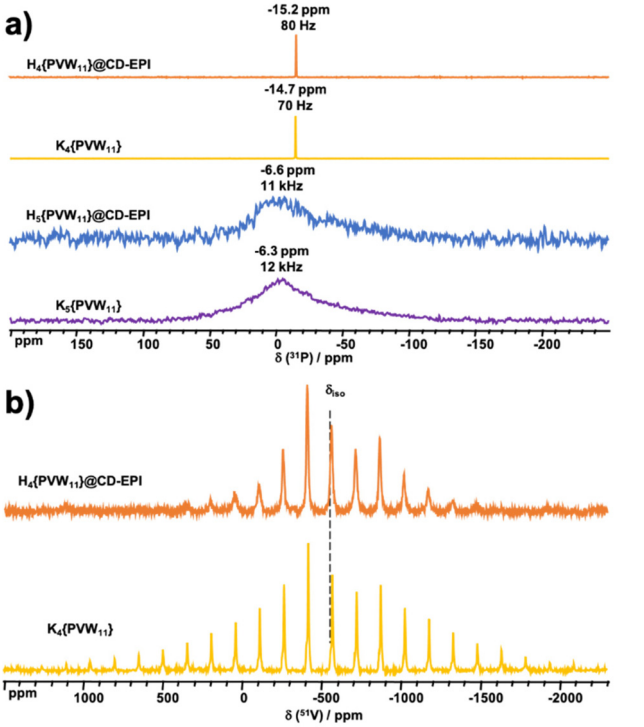

Fig. 6 (a) ^{31}P MAS NMR spectra of POM@CD–EPI composites compared with the spectra of the original POMs studied $K_5[PV^{IV}W_{11}O_{40}]\cdot16H_2O$ and $K_4[PV^{V}W_{11}O_{40}]\cdot9H_2O$. (b) ^{51}V MAS NMR spectrum of the POM@CD–EPI composite compared with the spectrum of the original POM compound $K_4[PV^{V}W_{11}O_{40}]\cdot9H_2O$.

Comparison of POM adsorption performance with the literature

Most previous studies on Keggin-type POM adsorption have been carried out on porous catalyst supports such as activated carbon and MOFs,[50–52] while, to our knowledge, no data can be found in the literature on polymeric materials. Wu *et al.* have studied in detail the adsorption properties of phospho- and silico-molybdate and -tungstate polyacids with the Keggin structure on various activated carbons and other porous materials.[52,53] More recently, MOFs have been shown as potential host materials to encapsulate POMs for a variety of purposes, such as catalysis, energy conversion or environmental remediation.[15,54–60] However, there are very few detailed quantitative studies on adsorption properties with these types of supports, such as adsorption isotherms and kinetics. Table 4 presents a comprehensive comparison and analysis of available q_{max} values for numerous adsorbents and Keggin-type POMs, including our results obtained with the CD–EPI polymer. The most effective adsorbent materials were porous activated carbons and bentonite, with exceptional loading capacity in the range of *ca.* 400–800 μmol g^{-1}.[52,61–63] It should

Table 4 Efficiency of different adsorbents towards Keggin-type POMs

POM	Adsorbent	q_{max} (μmol g^{-1})	Ref.
$H_3[PMo_{12}O_{40}]$	Titania	5	65
	Silica	11	65
	Carbon	11	65
	Alumina	15–130	51 and 65
	Bentonite	48	52
	MIL-101(Cr)	285	46
	Activated C	355–800	61–63
$H_3[PW_{12}O_{40}]$	Bentonite	53	52
	Zr_6-TCPP-Fe-120	95	64
	MIL-101(Fe)	139	60
	Zr_6-TCPP-120	165	64
	Activated C	330	50
$H_4[SiMo_{12}O_{40}]$	Silica	33	66
	Bentonite	33	52
	Carbon	36	66
	MIL-101(Cr)	279	46
	Activated C	285	53
$H_4[SiW_{12}O_{40}]$	Diatomite	3	52
	Titania	9	52
	Bentonite	37	52
	Alumina	139	52
	Activated C	200	52
$H_4[PV^{V}Mo_{11}O_{40}]$	MIL-101(Cr)	259	46
$(NH_4)_5[PV^{IV}Mo_{11}O_{40}]$	MIL-101(Cr)	210	46
$Na_3[PW_{12}O_{40}]$	CD–EPI polymer	135	This work
$K_4[PV^{V}W_{11}O_{40}]$	CD–EPI polymer	102	This work
$K_5[PV^{IV}W_{11}O_{40}]$	CD–EPI polymer	75	This work
$NaRb_5[H_2W_{12}O_{40}]$	CD–EPI polymer	90	This work

be mentioned, however, that this outstanding performance is achieved with phosphomolybdate POMs and that their tungsten POM counterparts have always shown much lower values (*ca.* 300 μmol g^{-1}).[50] Our results with the CD–EPI polymer range from 75 to 135 μmol g^{-1}, which is comparable to the adsorption performance of Keggin phosphotungstates on mesoporous MOF compounds showing values between 95 and 165 μmol g^{-1}.[60,64] However, for the same phosphotungstate POM family, our CD–EPI polymer showed a lower adsorption capacity than activated carbons, *i.e.*, 330 μmol g^{-1},[50] but much higher than that of aluminosilicate bentonite clay (53 μmol g^{-1}).[52] These comparisons demonstrate the excellent adsorption performance of our cyclodextrin-based polymer, similar to meso- and micro-porous solids such as MOFs, zeolites, or layered oxides. This suggests that the copolymerization of EPI with CD may generate mesoporosity within the polymeric network in conjunction with the preformed ring-shaped CD building blocks that would constitute local cavities for adsorption sites. The influence of POM's negative charge on adsorption capacity can also be significant considering that the chaotropic effect could contribute to the encapsulation process. Indeed, the general tendency shows that adsorption with $[PM_{12}O_{40}]^{3-}$ is always superior to that with $[SiM_{12}O_{40}]^{4-}$, and the same is true for $[PV^{V}M_{11}O_{40}]^{4-}$ compared to $[PV^{IV}M_{11}O_{40}]^{5-}$ (M = Mo or W).

Catalytic performance of the POM@CD–EPI composites

The catalytic activity of the POM@CD–EPI composites was tested in the oxidation of BnOH to BzOH, using hydrogen peroxide (H_2O_2) or *tert*-butyl hydroperoxide (*t*-BuOOH) as the oxidizing agents (Table 5). The presence of an oxidizing agent in conjunction with a catalyst is necessary to observe a decent conversion (Table 5, entries 16 and 17). Catalysis with POM-only systems (Table 5, entries 8–11) showed comparable conversion in the range of 40–50% and selectivity for BzOH around 60%, irrespective of the oxidizing agent or the initial oxidation state of V center (V^{V} or V^{IV}) in the POM. The situation is different for composites, and contrasting results have

Table 5 Oxidation of BnOH into BzH and BzOH with POM and POM@CD–EPI composites[a]

Entry	Oxidizing agent	Catalyst	Conversion[b] (%)	BzH yield[c] (%)	BzOH yield[c] (%)	BzOH selectivity[d] (%)
1	H_2O_2	$\{PW_{12}\}^{3-}$@CD–EPI[e]	99	1	98	99
2	H_2O_2	$\{PV^{V}W_{11}\}^{4-}$@CD–EPI[e]	30	9	21	70
3	H_2O_2	$\{PV^{IV}W_{11}\}^{5-}$@CD–EPI[e]	26	7	19	73
4	*t*-BuOOH	$\{PW_{12}\}^{3-}$@CD–EPI	4	1	3	75
5	*t*-BuOOH	$\{PV^{V}W_{11}\}^{4-}$@CD–EPI	95	5	90	95
6	*t*-BuOOH	$\{PV^{IV}W_{11}\}^{5-}$@CD–EPI	100	1	99	99
7	*t*-BuOOH	$\{H_2W_{12}\}^{6-}$@CD–EPI	58	15	43	74
8	H_2O_2	$K_4[PV^{V}W_{11}O_{40}]$	43	17	26	60
9	*t*-BuOOH	$K_4[PV^{V}W_{11}O_{40}]$	49	18	31	63
10	H_2O_2	$K_5[PV^{IV}W_{11}O_{40}]$	46	17	29	63
11	*t*-BuOOH	$K_5[PV^{IV}W_{11}O_{40}]$	86	9	77	90
12	H_2O_2	$K_5[PV^{IV}W_{11}O_{40}]$ + 1 eq. CD	58	9	48	84
13	*t*-BuOOH	$K_5[PV^{IV}W_{11}O_{40}]$ + 1 eq. CD	99	1	98	99
14	*t*-BuOOH	$K_5[PV^{IV}W_{11}O_{40}]$ + 2 eq. CD	66	20	46	70
15	*t*-BuOOH	$K_5[PV^{IV}W_{11}O_{40}]$ + 5 eq. CD	21	13	8	38
16	No oxidant	$\{PV^{IV}W_{11}\}^{5-}$@CD–EPI	1	1	0	0
17	*t*-BuOOH	No catalyst	4	4	0	0

[a] Reaction conditions: 2 mmol of substrate (BnOH), 12.5 mmol of oxidizing agent (H_2O_2 or *t*-BuOOH), 0.01 mmol of catalyst (POM), 60 °C, 24 h. [b] C (%) = $(1 - f_{BnOH}) \times 100$. [c] $Y_{product}$ (%) = $f_{product} \times 100$. [d] S_{BzOH} (%) = $f_{BzOH} \times 100/(f_{BzOH} + f_{BzH})$; f = molar fraction. [e] POM leaching/catalyst degradation.

been obtained depending on the oxidizing agent used and the nature of the POM in the polymer. With H_2O_2, the best performance was achieved with $\{PW_{12}\}^{3-}$@CD–EPI, showing full conversion and selectivity (Table 5, entry 1), but reaction in this medium led to catalyst degradation and POM release. Indeed, the coloration of the collected product (yellow/brown) and the ^{31}P and ^{51}V NMR analyses clearly indicated the leaching of the POM (see Fig. S15†). In the case of *t*-BuOOH, the products obtained were always colorless and no catalyst degradation was observed. Surprisingly, the catalytic activity of the composites was reversed with this oxidant, *i.e.*, $\{PW_{12}\}^{3-}$@CD–EPI became inactive (Table 5, entry 4), and the vanadium-containing POM composites $\{PVW_{11}\}^{4/5-}$@CD–EPI were highly efficient (Table 5, entries 5 and 6). These results seem to indicate that oxidation with H_2O_2 leads to degradation of the composites, while reactions with *t*-BuOOH preserve their integrity. Consequently, the system with *t*-BuOOH is preferred over that with H_2O_2. Moreover, with composites, the separation of the catalyst from the products is easy, offering the possibility of recycling, which is not possible in homogeneous POM-only catalysis. We also note the same performance of both POMs regardless of their charge (4− or 5−) in the composite, as was observed with the POM catalyst alone. This means that the large excess of oxidizing agent continuously regenerates the oxidized POM during the catalytic process, whether starting from the oxidized or reduced form. No special precautions are therefore necessary to protect the catalysts from ambient oxidation. Regarding the effect of cyclodextrin, further experiments were carried out with a physical mixture of the catalyst $K_5[PV^{IV}W_{11}O_{40}]$ and free γ-CD up to 5 eq. (Table 5, entries 12–15). In these cases, the catalysis is no longer homogeneous, as cyclodextrin was not soluble in these reaction mixtures. Part of the POM remains in the liquid phase as indicated by its color. In the presence of one eq. of CD relative to POM, excellent performance in terms of conversion and selectivity was observed with *t*-BuOOH, but not with H_2O_2. However, increasing the amount of CD led to a decrease in catalytic performance. Clearly, a large excess of CD inhibits POM activity in these molecular systems, probably due to the screening effect. It can be noticed that for POM–polymer, even with a CD/POM molar ratio close to 5, the catalytic activity is high, demonstrating the importance of the dispersion of CD inside the polymer.

These initial results show that the best catalytic system is the tandem $\{PVW_{11}\}^{4/5-}$@CD–EPI composites and *t*-BuOOH as the catalyst and oxidizing agent, respectively. Therefore, we focused on the $\{PV^{IV}W_{11}\}^{5-}$@CD–EPI/*t*-BuOOH system to study and optimize the experimental conditions. Fig. 7 summarizes the results obtained from investigations into the effects of temperature, solvent, and substrate quantity, as well as kinetics and recyclability studies. Although the catalytic performance obtained at 60 °C/24 h is quite good, we attempted to reduce the reaction time by increasing the temperature. However, we observed that increasing the reaction temperature is accompanied by catalyst degradation, manifested by POM release and polymer degradation. Fig. 7a shows the best catalytic performance just before catalyst degradation for different temperatures. The higher the temperature, the shorter the

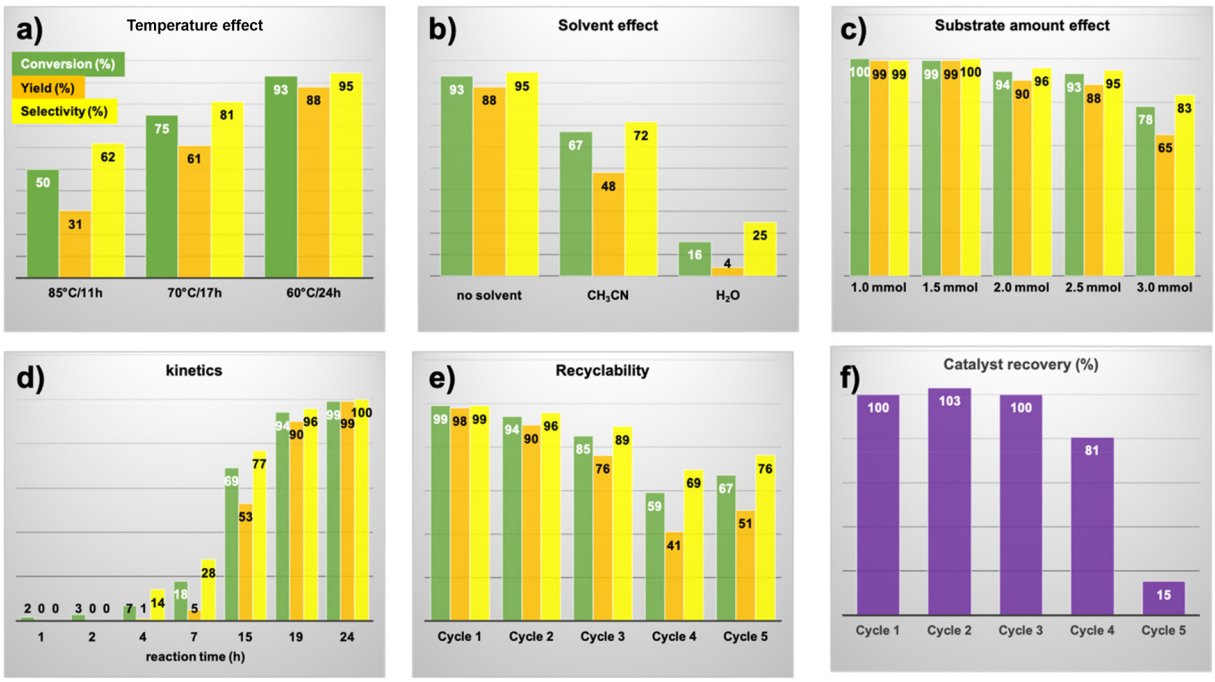

Fig. 7 Oxidation of benzyl alcohol to benzoic acid with $\{PV^{IV}W_{11}\}^{5-}$@CD–EPI using *t*-BuOOH as the oxidizing agent: (a) temperature effect, (b) solvent effect, (c) substrate amount effect, (d) kinetic study, and (e and f) recyclability study. Reaction conditions when not indicated: 2.5 mmol substrate in (a) and (b) or 1.5 mmol substrate in (d)–(f), 12.5 mmol oxidizing agent, 0.01 mmol POM, 1 mL solvent, 60 °C, 24 h.

reaction time and the lower the conversion and selectivity. We conclude that 60 °C/24 h is the optimum reaction condition without catalyst degradation. Fig. 7b shows the results of adding extra solvent (1 mL) to the reaction medium. Performance is significantly lower in the presence of acetonitrile, and even poorer with additional water. By varying the amount of the substrate from 1 to 3 mmol, we can see from Fig. 7c that the lower the amount, the higher the catalytic performance, achieving full conversion and selectivity at 1.5 mmol BnOH. The kinetic study is therefore carried out with this optimal amount of substrate and illustrated in Fig. 7d. The reaction gets off to a slow start since it is only after 7 h of reaction that significant conversion is recorded with very low selectivity (<50%), meaning that the prominent product at this stage is benzaldehyde. This proves that the oxidation to benzoic acid is a two-step process *via* benzaldehyde. Finally, tests on the recyclability of the catalyst recovered by simple separation of the reaction mixture by centrifugation are shown in Fig. 7e and f. The same starting catalyst was successfully used up to five runs. During the first three cycles, there is no apparent degradation of the catalyst, the liquid part of the reaction medium was colorless and there was no weight loss of the recovered solid (Fig. 7f). Nevertheless, there is a slight, steady decline in performance. After the fourth run, we observe a significant drop in conversion and selectivity as a result of catalyst degradation, observed by a 20% weight loss and the yellow product coloring (see Fig. 8f and the next section). After five runs, only 15% of the initial catalyst is recovered due to advanced oxidation of the polymer backbone, despite the preservation of a certain catalytic performance.

In summary, our $\{PV^{IV}W_{11}\}^{5-}$@CD–EPI composite exhibits excellent catalytic activity for the oxidation of benzyl alcohol to benzoic acid with *t*-BuOOH and can be compared with other reported tungsten-POM-based catalysts (Table 6). In comparison with the literature, only two systems showed such good results for benzoic acid as the final product. The former is a silver-containing POM framework effective under aerobic conditions in photocatalysis,[67] while the latter is a supramolecular complex with β-CD $\{3CD@SiW_{12}\}$ used in H_2O_2.[25] The TON and TOF values of 125 and 5 h^{-1}, respectively, for our $\{PV^{IV}W_{11}\}^{5-}$@CD–EPI catalyst are within the typical ranges reported. Most other work on this catalysis has reported rather high selectivity for benzaldehyde.[68–74] We also note that H_2O_2 is the oxidizing agent most commonly used for this reaction, and that the temperature is generally high, between 85 and 110 °C. Although the most widely used tungsten-based Keggin catalysts are phosphododecatungstate $\{PW_{12}\}$, a few examples of mixed vanadotungstate POMs have also been reported in the catalytic oxidation of benzyl alcohol.[75–78] In all these studies, selectivity was once again exclusive to benzaldehyde.

Stability of POM@CD–EPI composites during catalysis

To gain further insights into the stability of the composite after catalysis, NMR analyses of the catalyst and the reaction medium were performed after successive cycles, as shown in Fig. 8. Solid-state NMR spectra (^{51}V and ^{31}P) of the catalyst

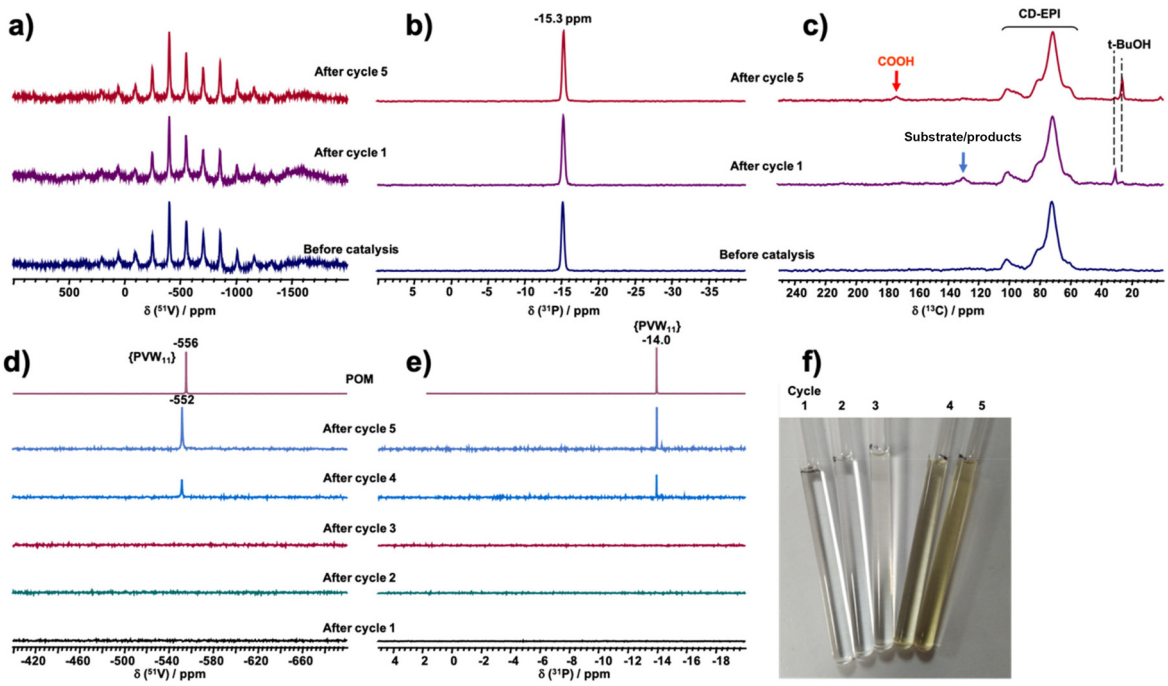

Fig. 8 Solid-state (a) ^{51}V MAS, (b) ^{31}P MAS, and (c) $^{13}C\{^1H\}$ CPMAS NMR spectra of the catalyst before ($\{PV^{V}W_{11}\}^{4-}$@CD–EPI) and after catalysis ($\{PV^{IV}W_{11}\}^{5-}$@CD–EPI). Liquid-state (d) ^{51}V and (e) ^{31}P NMR spectra of the liquid part of the reaction medium in CD_3CN compared to the spectra of the starting POM $K_4[PV^{V}W_{11}O_{40}]$ in D_2O. (f) Photographs of the NMR tubes of (d) and (f). Reaction conditions of one cycle: 1.5 mmol substrate, 12.5 mmol oxidizing agent *t*-BuOOH, 0.01 mmol POM in the catalyst, 60 °C, 24 h.

Table 6 Comparison with the literature of the performance of the $\{PV^{IV}W_{11}\}^{5-}$@CD–EPI catalyst in the oxidation of benzyl alcohol (BnOH) to benzoic acid (BzOH)

Catalyst	Oxidant	T (°C)/t (h)	Conversion (%)	Selectivity, BzOH (%)	TON[a]	TOF[b] (h^{-1})	Ref.
$\{PV^{IV}W_{11}\}^{5-}$@CD–EPI	*t*-BuOOH	60 °C/24 h	99	100	124	5	This work
$[Ag_3L_2(OH)]\{PW_{12}\}^{c}$	λ 365 nm[g]	RT/12 h	99	99	10	1	67
$\{3\beta\text{-CD@SiW}_{12}\}$	H_2O_2	85 °C/24 h	96	97	233	10	25
$[L]_7\{PW_{11}\}^{d}$	H_2O_2	85 °C/7 h	99	58	72	10	79
$\{NiSiW_{12}\}$	H_2O_2	90 °C/3.5 h	34	38	37	10	69
$\{PW_{12}\}$@MC[e]	H_2O_2	95 °C/5 h	92	31	36	7	70
$Ce_{0.66}H\{PW_{12}\}$	H_2O_2	110 °C/4 h	96	26	173	43	73
MimAM(H)-$\{PW_{12}\}^{f}$	H_2O_2	90 °C/0.5 h	100	17	53	106	72
$\{BW_{11}\}$	H_2O_2	90 °C/6 h	98	16	10	2	68
$Py_3\{PW_{12}\}$	H_2O_2	90 °C/2 h	33	19	21	10	71
$H_3\{PW_{12}\}$	H_2O_2	90 °C/15 h	96	10	19	1	74

[a] TON = moles of BzOH produced/moles of POM. [b] TOF = TON/t (h). [c] L = 1,4-di(4*H*-1,2,4-triazol-4-yl). [d] L = $N(C_{18}H_{37})_2(CH_3)_2$. [e] MC = mesoporous carbon. [f] MimAM = 1-aminoethyl-3-methylimidazolium. [g] Photocatalysis.

before and after one and five uses showed identical spectra indicating the preservation of the integrity of the POM structure in the composite throughout the five catalytic cycles. In ^{13}C NMR, we also observe the same resonances of the starting polymer, again indicating no major deterioration of the polymer matrix. We observe, however, small additional resonances due to the presence of residual reactants and products still absorbed, *e.g.*, *t*-BuOOH/*t*-BuOH, BnOH, and BzOH. This may explain the slight increase in recovered catalyst weight in some cases exceeding 100% recovery (Fig. 7f). These results confirm the relative robustness of the composite and its resistance to the catalytic conditions studied (*t*-BuOOH, 60 °C/24 h). In the liquid phase, no signals were detected in ^{51}V or ^{31}P NMR up to three cycles (Fig. 8d and e), but the POM $\{PV^{V}W_{11}\}^{4-}$ resonances start to appear in the fourth cycle and continue to increase in the fifth cycle. ICP analyses are also consistent with POM leaching only after four catalytic cycles (see Table S3, ESI†). This is consistent with the yellowish color of the products (Fig. 8f), with loss of recovered catalyst (Fig. 7e), and with the degrease in catalytic performance (Fig. 7f). This means that the catalyst deterioration results from leaching of the POM units, most likely following the degradation of the polymer backbone. This latter also contains alcohol functions from the cyclodextrin and glycerol moieties and is therefore subject to oxidative attack. It is worth noting that, when using H_2O_2 or POM as a catalyst instead of the composite, the POM is degraded and other species are formed (see Fig. S15c and S15d, ESI†).

Mechanisms and reaction pathways

On the basis of the experimental results and observations made above, we propose in Fig. 9 the mechanisms based on the unique host–guest supramolecular properties of CD to explain the remarkable catalytic activity of our POM@CD–EPI

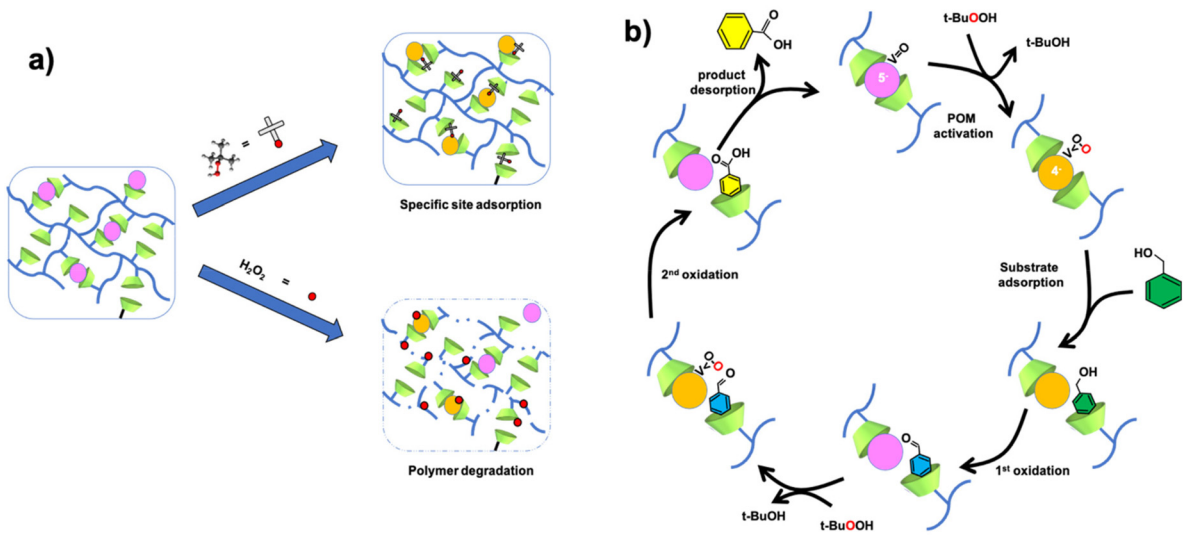

Fig. 9 Proposed mechanisms based on the host–guest supramolecular effect of CD to (a) prevent degradation of the polymer backbone and to (b) drive the oxidation process of BnOH selectively to BzOH.

composite with the oxidizing agent *t*-BuOOH regarding (i) its structural stability and integrity and (ii) its selectivity for the oxidation of benzyl alcohol to benzoic acid. The key point here is the hydrophobic bulky character of the *tert*-butyl moiety of the oxidizing agent. First, concerning the stability of the composite (Fig. 9a), in the presence of the CD-based polymer, *t*-BuOOH should be adsorbed specifically into the CD cavity, under the effect of a hydrophobic repulsion force. ^{13}C NMR (Fig. 8c) showed indeed the adsorption of some *t*-BuOOH/*t*-BuOH in the catalyst. The CD/POM molar ratio is about five, suggesting that the composite should contain many free CDs as potential interaction sites. Moreover, the hydrophobic character of *t*-BuOOH can prevent its approach to the organic part (polymer backbone) of the composite, while this is not the case with the smaller and hydrophilic H_2O_2. The oxidative attack of the latter on the numerous hydroxyl groups of the glycerol fragments then becomes very favorable, thus weakening the polymer matrix of the composite and consequently the adhesion of the POM. Therefore, the use of a weak oxidant like *t*-BuOOH becomes advantageous here to avoid overoxidation of the polymer.

Once adsorbed, *t*-BuOOH must be sufficiently close to the POM deeply embedded in the polymer matrix, thus facilitating its activation. For this to occur, *t*-BuOOH needs to diffuse into the polymer matrix of the composite, which explains the induction time of 2–4 h observed in the kinetic study (Fig. 7d). In addition, solid-state NMR of the recovered catalyst, shown in Fig. 8c, also indicates the presence of occluded *t*-BuOOH/*t*-BuOH species despite intensive washing. Fig. 9b schematically shows the catalytic cycle taking place inside the POM–polymer composite. It is well established that vanadium plays a key role in the activation of the POM by lowering its redox potentials.[78] The postulated active species is therefore a vanadoperoxo complex that provides active oxygen.[80,81] Because cyclodextrins constitute the anchoring sites for POM species and also for *t*-BuOOH, the catalytic process is governed as a whole by supramolecular chemistry in a confined environment. Indeed, the diffusion and molecular approach of the substrate should occur through its hydrophobic part, *i.e.*, its aromatic ring, to form host–guest complexes with the central cavity of CDs without dissociating the POMs from the polymer host. Oxidation of substrates taking place inside the POM–polymer composite in a confined environment is expected to be more efficient than a reaction with dissociated free CD and POM molecular constituents. This may explain why a second consecutive oxidation occurs immediately after the first one to produce the final benzoic acid product. Confined reactions have several advantages, including (i) acceleration of the catalytic process by favorizing molecular contact and, more interestingly, (ii) promotion of cascade reactions through the steric effect which improves selectivity. It appears that the beneficial role of CD lies in its ability to promote supramolecular complexation not only with organic molecules (*t*-BuOOH and the substrate) through its well-known hydrophobic effect, but also with inorganic POMs through its newly discovered chaotropic effect.

Conclusions

In this research, we present a detailed quantitative study of the adsorption process of polyoxometalates on a γ-CD-based polymer, including adsorption isotherms and kinetics. The polymer resulting from the copolymerization of γ-CD with EPI showed high affinity towards POMs of the Keggin structure. The integrity of the POM structure and the preservation of its chemical composition in the hybrids were verified using solid-state NMR, FT-IR spectroscopy and elemental analyses. The maximum adsorption capacity (q_{max}) was estimated between 75 and 135 μmol g^{-1}, depending on the negative charge of the POM, *i.e.*, the lower the charge, the higher the q_{max}. Such a trend suggests an adsorption mechanism driven by the chaotropic effect, where the solvation properties of the POM depend strongly on the charge density at its surface. These q_{max} values match the typical adsorption performance observed with mesoporous materials such as MOFs. The potential of CD–EPI polymers as alternative supports for POM heterogenization is evaluated in the selective oxidation of benzyl alcohol. The bulky and hydrophobic oxidizing agent *t*-BuOOH was found to be the best partner of {PVW_{11}}@CD–EPI to form an efficient catalytic tandem for the oxidation of benzyl alcohol to benzoic acid. The host–guest supramolecular properties of CD are key parameters for not only improving the catalyst stability but also improving the catalytic performances through reactions in a confined environment. With these promising results, our team is now focusing on using the γ-CD-based polymer as a hosting matrix to entrap complementary functional building units to design photo-catalytic systems or tandem catalysis.

Conflicts of interest

There are no conflicts to declare.

Data availability

The authors confirm that the data supporting the findings of this study are available within the article and its ESI.†

Acknowledgements

This work is supported by the "Investissements d'Avenir" program (Labex Charm3at, ANR-11-LABX-0039-grant). The CNRS and the University of Versailles Saint-Quentin are acknowledged for their financial supports. The authors thank Dr Ruxandra Gref from the Université Paris-Saclay for her advice on the synthesis of CD–EPI based polymers. SA thanks CampusFrance for the Excellence Eiffel doctoral grant.

References

1 N. I. Gumerova and A. Rompel, Polyoxometalates in Solution: Speciation under Spotlight, *Chem. Soc. Rev.*, 2020, **49**(21), 7568–7601, DOI: 10.1039/d0cs00392a.

2 A. Maalaoui, H. Guedidi, M. Rzaigui and S. Akriche, Aldehyde-Assisted Aerobic-Oxidative Desulfurization of HDS Diesel Fuels by a Highly Effective Heterogeneous V-Substituted Keggin-Type Semiorganic Catalyst: Modeling of Experimental Design and Mechanistic and Kinetic Insights, *Energy Fuels*, 2024, **38**(2), 1319–1329, DOI: 10.1021/acs.energyfuels.3c04332.

3 Y. Nakagawa, K. Kamata, M. Kotani, K. Yamaguchi and N. Mizuno, Polyoxovanadometalate-Catalyzed Selective Epoxidation of Alkenes with Hydrogen Peroxide, *Angew. Chem., Int. Ed.*, 2005, **44**(32), 5136–5141, DOI: 10.1002/anie.200500491.

4 B. E. Petel and E. M. Matson, Oxygen-Atom Vacancy Formation and Reactivity in Polyoxovanadate Clusters, *Chem. Commun.*, 2020, **56**(88), 13477–13490, DOI: 10.1039/D0CC05920J.

5 Y. Seki, N. Mizuno and M. Misono, Catalytic Performance of 11-Molybdo-1-Vanadophosphoric Acid as a Catalyst Precursor and the Optimization of Reaction Conditions for the Oxidation of Methane with Hydrogen Peroxide, *Appl. Catal., A*, 2000, **194–195**, 13–20, DOI: 10.1016/S0926-860X(99)00348-8.

6 A. Anyushin, A. Kondinski and T. N. Parac-Vogt, Hybrid Polyoxometalates as Post-Functionalization Platforms: From Fundamentals to Emerging Applications, *Chem. Soc. Rev.*, 2020, **49**(2), 382–432, DOI: 10.1039/c8cs00854j.

7 A. Ebrahimi, L. Krivosudsky, A. Cherevan and D. Eder, Polyoxometalate-Based Porphyrinic Metal-Organic Frameworks as Heterogeneous Catalysts, *Coord. Chem. Rev.*, 2024, **508**, 215764, DOI: 10.1016/j.ccr.2024.215764.

8 R. Kawahara, K. Niinomi, J. N. Kondo, M. Hibino, N. Mizuno and S. Uchida, A Functional Mesoporous Ionic Crystal Based on Polyoxometalate, *Dalton Trans.*, 2016, **45**(7), 2805–2809, DOI: 10.1039/C5DT04556H.

9 Y. Martinetto, B. Pegot, C. Roch-Marchal, B. Cottyn-Boitte and S. Floquet, Designing Functional Polyoxometalate-Based Ionic Liquid Crystals and Ionic Liquids, *Eur. J. Inorg. Chem.*, 2019, 21, DOI: 10.1002/ejic.201900990.

10 P. Ma, F. Hu, J. Wang and J. Niu, Carboxylate Covalently Modified Polyoxometalates: From Synthesis, Structural Diversity to Applications, *Coord. Chem. Rev.*, 2019, **378**, 281–309, DOI: 10.1016/j.ccr.2018.02.010.

11 J. J. Stracke and R. G. Finke, Distinguishing Homogeneous from Heterogeneous Water Oxidation Catalysis When Beginning with Polyoxometalates, *ACS Catal.*, 2014, **4**(3), 909–933, DOI: 10.1021/cs4011716.

12 G. Chen, Y. Zhou, Z. Long, X. Wang, J. Li and J. Wang, Mesoporous Polyoxometalate-Based Ionic Hybrid As a Triphasic Catalyst for Oxidation of Benzyl Alcohol with H_2O_2 on Water, *ACS Appl. Mater. Interfaces*, 2014, **6**(6), 4438–4446, DOI: 10.1021/am5001757.

13 K. Maru, S. Kalla and R. Jangir, MOF/POM Hybrids as Catalysts for Organic Transformations, *Dalton Trans.*, 2022, **51**, 11952–11986, DOI: 10.1039/d2dt01895k.

14 A. Misra, I. F. Castillo, D. P. Müller, C. González, S. Eyssautier-Chuine, A. Ziegler, J. M. de la Fuente, S. G. Mitchell and C. Streb, Polyoxometalate-Ionic Liquids (POM-ILs) as Anticorrosion and Antibacterial Coatings for Natural Stones, *Angew. Chem., Int. Ed.*, 2018, **57**(45), 14926–14931, DOI: 10.1002/anie.201809893.

15 J. Sun, S. Abednatanzi, P. Van Der Voort, Y.-Y. Liu and K. Leus, POM@MOF Hybrids: Synthesis and Applications, *Catalysts*, 2020, **10**(5), 578, DOI: 10.3390/catal10050578.

16 I. Ullah, A. Munir, A. Haider, N. Ullah and I. Hussain, Supported Polyoxometalates as Emerging Nanohybrid Materials for Photochemical and Photoelectrochemical Water Splitting, *Nanophotonics*, 2021, **10**(6), 1595–1620, DOI: 10.1515/nanoph-2020-0542.

17 J. Simons, N. Hazra, A. V. Petrunin, J. J. Crassous, W. Richtering and M. Hohenschutz, Nonionic Microgels Adapt to Ionic Guest Molecules: Superchaotropic Nanoions, *ACS Nano*, 2024, **18**, 7546–7557, DOI: 10.1021/acsnano.3c12357.

18 C. Mu, Y. Chen, Z. Dai, W. Li, J. Wang, X. Jiao, D. Chen and T. Wang, Pom Functionalized Ionogels with Tunable Optical, Mechanical, Electrical, and Sensory Properties, *Adv. Funct. Mater.*, 2023, 2313957, DOI: 10.1002/adfm.202313957.

19 W. Salomon, Y. H. Lan, E. Riviere, S. Yang, C. Roch-Marchal, A. Dolbecq, C. Simonnet-Jegat, N. Steunou, N. Leclerc-Laronze, L. Ruhlmann, T. Mallah, W. Wernsdorfer and P. Mialane, Single-Molecule Magnet Behavior of Individual Polyoxometalate Molecules Incorporated within Biopolymer or Metal-Organic Framework Matrices, *Chem. – Eur. J.*, 2016, **22**(19), 6564–6574, DOI: 10.1002/chem.201600202.

20 S. Yao, C. Falaise, A. A. Ivanov, N. Leclerc, M. Hohenschutz, M. Haouas, D. Landy, M. A. Shestopalov, P. Bauduin and E. Cadot, Hofmeister Effect in the Keggin-Type Polyoxotungstate Series, *Inorg. Chem. Front.*, 2021, **8**(1), 12–25, DOI: 10.1039/d0qi00902d.

21 S. Khlifi, S. Yao, C. Falaise, P. Bauduin, V. Guerineau, N. Leclerc, M. Haouas, H. Salmi-Mani, P. Roger and E. Cadot, Switchable Redox and Thermo-Responsive Supramolecular Polymers Based on Cyclodextrin-Polyoxometalate Tandem, *Chem. – Eur. J.*, 2024, **30**, e202303815, DOI: 10.1002/chem.202303815.

22 S. Yao, C. Falaise, N. Leclerc, C. Roch-Marchal, M. Haouas and E. Cadot, Improvement of the Hydrolytic Stability of the Keggin Molybdo- and Tungsto-Phosphate Anions by Cyclodextrins, *Inorg. Chem.*, 2022, **61**(9), 4193–4203, DOI: 10.1021/acs.inorgchem.2c00095.

23 Y. Fan, Y. Zhang, Q. Jia, J. Cao and W. Wu, The Stabilizing Role of Cyclodextrins on Keggin Phosphotungstic Acid by Complexation Unveiled by Electrospray Mass Spectrometry, *Mass Spectrom. Lett.*, 2015, **6**(1), 13–16, DOI: 10.5478/MSL.2015.6.1.13.

24 Z. Zhu, M. Wei, B. Li and L. Wu, Constructing Chiral Polyoxometalate Assemblies via Supramolecular Approaches, *Dalton Trans.*, 2021, **50**(15), 5080–5098, DOI: 10.1039/d1dt00182e.
25 L. Ni, H. Li, H. Xu, C. Shen, R. Liu, J. Xie, F. Zhang, C. Chen, H. Zhao, T. Zuo and G. Diao, Self-Assembled Supramolecular Polyoxometalate Hybrid Architecture as a Multifunctional Oxidation Catalyst, *ACS Appl. Mater. Interfaces*, 2019, **11**(42), 38708–38718, DOI: 10.1021/acsami.9b12531.
26 S. Khlifi, J. Marrot, M. Haouas, W. E. Shepard, C. Falaise and E. Cadot, Chaotropic Effect as an Assembly Motif to Construct Supramolecular Cyclodextrin-Polyoxometalate-Based Frameworks, *J. Am. Chem. Soc.*, 2022, **144**(10), 4469–4477, DOI: 10.1021/jacs.1c12049.
27 P. Yang, W. Zhao, A. Shkurenko, Y. Belmabkhout, M. Eddaoudi, X. Dong, H. N. Alshareef and N. M. Khashab, Polyoxometalate-Cyclodextrin Metal-Organic Frameworks: From Tunable Structure to Customized Storage Functionality, *J. Am. Chem. Soc.*, 2019, **141**(5), 1847–1851, DOI: 10.1021/jacs.8b11998.
28 B. Gidwani and A. Vyas, A Comprehensive Review on Cyclodextrin-Based Carriers for Delivery of Chemotherapeutic Cytotoxic Anticancer Drugs, *BioMed. Res. Int.*, 2015, 98268, DOI: 10.1155/2015/198268.
29 M. Komiyama, Monomeric, Oligomeric, Polymeric, and Supramolecular Cyclodextrins as Catalysts for Green Chemistry, *Research*, 2024, **7**, 0466, DOI: 10.34133/research.0466.
30 X. Liu, J. Zhang, Y. Lan, Q. Zheng and W. Xuan, Infinite Building Blocks for Directed Self-Assembly of a Supramolecular Polyoxometalate-Cyclodextrin Framework for Multifunctional Oxidative Catalysis, *Inorg. Chem. Front.*, 2022, **9**, 6534–6543, DOI: 10.1039/d2qi02085h.
31 S. Sadjadi, A. M. Rezadoust, S. Yaghoubi, E. Monflier and A. Heydari, 3D-Printed Cyclodextrin Polymer Encapsulated Wells-Dawson: A Novel Catalyst for Knoevenagel Condensation Reactions, *ACS Omega*, 2023, **8**(48), 45844–45853, DOI: 10.1021/acsomega.3c06592.
32 C. Falaise, S. Khlifi, P. Bauduin, P. Schmid, J. Degrouard, A. Leforestier, W. Shepard, J. Marrot, M. Haouas, D. Landy, C. Mellot-Draznieks and E. Cadot, Cooperative Self-Assembly Process Involving Giant Toroidal Polyoxometalate as a Membrane Building Block in Nanoscale Vesicles, *J. Am. Chem. Soc.*, 2024, **146**(2), 1501–1511, DOI: 10.1021/jacs.3c11004.
33 M. Hohenschutz, P. Bauduin, C. G. Lopez, B. Foerster and W. Richtering, Superchaotropic Nano-Ion Binding as a Gelation Motif in Cellulose Ether Solutions, *Angew. Chem., Int. Ed.*, 2023, **62**, e202210208, DOI: 10.1002/anie.202210208.
34 A. Malinenko, A. Jonchère, L. Girard, S. Parrès-Maynadié, O. Diat and P. Bauduin, Are Keggin's POMs Charged Nanocolloids or Multicharged Anions?, *Langmuir*, 2018, **34**(5), 2026–2038, DOI: 10.1021/acs.langmuir.7b03640.
35 A. Romo, F. J. Peñas, X. Sevillano and J. R. Isasi, Application of Factorial Experimental Design to the Study of the Suspension Polymerization of β-Cyclodextrin and Epichlorohydrin, *J. Appl. Polym. Sci.*, 2006, **100**(4), 3393–3402, DOI: 10.1002/app.23778.
36 E. Renard, A. Deratani, G. Volet and B. Sebille, Preparation and Characterization of Water Soluble High Molecular Weight Beta-Cyclodextrin-Epichlorohydrin Polymers, *Eur. Polym. J.*, 1997, **33**(1), 49–57, DOI: 10.1016/S0014-3057(96)00123-1.
37 G. Crini, C. Cosentino, S. Bertini, A. Naggi, G. Torri, C. Vecchi, L. Janus and M. Morcellet, Solid State NMR Spectroscopy Study of Molecular Motion in Cyclomaltoheptaose (β-Cyclodextrin) Crosslinked with Epichlorohydrin, *Carbohydr. Res.*, 1998, **308**(1–2), 37–45, DOI: 10.1016/S0008-6215(98)00077-9.
38 I. Mallard, D. Baudelet, F. Castiglione, M. Ferro, W. Panzeri, E. Ragg and A. Mele, Polydisperse Methyl β-Cyclodextrin-Epichlorohydrin Polymers: Variable Contact Time ^{13}C CP-MAS Solid-State NMR Characterization, *Beilstein J. Org. Chem.*, 2015, **11**, 2785–2794, DOI: 10.3762/bjoc.11.299.
39 J. A. Pellicer, M. I. Rodriguez-Lopez, M. I. Fortea, V. M. Gomez-Lopez, D. Aunon, E. Nunez-Delicado and J. A. Gabaldon, Synthesis of New Cyclodextrin-Based Adsorbents to Remove Direct Red 83:1, *Polymers*, 2020, **12**(9), 1880, DOI: 10.3390/polym12091880.
40 D. Rusu, O. Baban, I. Hauer, D. Gligor, L. David and M. Rusu, Synthesis and Characterization of the Potassium 11-Tungstovanado(IV) Phosphate, *Rev. Roum. Chim.*, 2010, **55**(11–12), 843–850.
41 X. Lu, T. Cheng, Y. V. Geletii, J. Bacsa and C. L. Hill, Reactivity and Stability Synergism Directed by the Electron Transfer between Polyoxometalates and Metal-Organic Frameworks, *Catal. Sci. Technol.*, 2023, **13**, 5094–5103, DOI: 10.1039/d3cy00569k.
42 Y.-S. Ho, Review of Second-Order Models for Adsorption Systems, *J. Hazard. Mater.*, 2006, **136**(3), 681–689, DOI: 10.1016/j.jhazmat.2005.12.043.
43 J. Wang and X. Guo, Adsorption Kinetic Models: Physical Meanings, Applications, and Solving Methods, *J. Hazard. Mater.*, 2020, **390**, 122156, DOI: 10.1016/j.jhazmat.2020.122156.
44 J. A. Pellicer, M. I. Rodriguez-Lopez, M. I. Fortea, J. A. G. Hernandez, C. Lucas-Abellan, M. T. Mercader-Ros, A. Serrano-Martinez, E. Nunez-Delicado, P. Cosma, P. Fini, E. Franco, R. Garcia, M. Ferrandiz, E. Perez and M. Ferrandiz, Removing of Direct Red 83:1 Using α- and HP-α-CDs Polymerized with Epichlorohydrin: Kinetic and Equilibrium Studies, *Dyes Pigm.*, 2018, **149**, 736–746, DOI: 10.1016/j.dyepig.2017.11.032.
45 C. Rocchiccoioli-Deltcheff, M. Fournier, R. Franck and R. Thouvenot, Vibrational Investigations of Popyoxometalates .2. Evidence for Anion Anion Interactions in Molybdenum(VI) and Tungsten(VI) Compounds Related to the Keggin Structure, *Inorg. Chem.*, 1983, **22**(2), 207–216, DOI: 10.1021/ic00144a006.
46 R. Canioni, C. Roch-Marchal, M. Haouas, A. Vimont, P. Horcajada, F. Sécheresse and C. Serre, MIL-101(Cr) MOF

as a Support for Reactive Polyoxometalates (POMs) Clusters. Principles of POMs Encapsulation and Chemistry of POMs Inside MIL-101 Cavities, *Curr. Inorg. Chem.*, 2017, **7**, 145–156, DOI: **10.2174/1877944107666171102141415**.

47 J. Juan-Alcaniz, M. G. Goesten, E. V. Ramos-Fernandez, J. Gascon and F. Kapteijn, Towards Efficient Polyoxometalate Encapsulation in MIL-100(Cr): Influence of Synthesis Conditions, *New J. Chem.*, 2012, **36**(4), 977–987, DOI: **10.1039/c2nj20587d**.

48 R. P. F. de Bonfim, L. C. de Moura, H. Pizzala, S. Caldarelli, S. Paul, J. G. Eon, O. Mentre, M. Capron, L. Delevoye and E. Payen, Synthesis and Structural Characterization of a New Nanoporous-like Keggin Heteropolyanion Salt: K3 $(H_2O)4[H_2SiVW11O40](H_2O)8+x$, *Inorg. Chem.*, 2007, **46**(18), 7371–7377, DOI: **10.1021/ic700384m**.

49 D. Massiot, F. Fayon, M. Capron, I. King, S. Le Calve, B. Alonso, J. Durand, B. Bujoli, Z. Gan and G. Hoatson, Modelling One- and Two-Dimensional Solid-State NMR Spectra, *Magn. Reson. Chem.*, 2002, **40**(1), 70–76, DOI: **10.1002/mrc.984**.

50 M. Schwegler, P. Vinke, M. Van Dereijk and H. Van bekkum, Activated Carbon as a Support For Heteropolyanion Catalysts, *Appl. Catal., A*, 1992, **80**(1), 41–57, DOI: **10.1016/0926-860X(92)85107-M**.

51 M. A. Castillo, P. G. Vazquez, M. N. Blanco and C. V. Caceres, Adsorption Studies and Species Characterization in Catalysts Obtained from Aqueous Solutions or Phosphomolybdic Acid and Gamma-Alumina, *J. Chem. Soc., Faraday Trans.*, 1996, **92**(17), 3239–3246, DOI: **10.1039/ft9969203239**.

52 Y. Wu, X. K. Ye, X. G. Yang, X. P. Wang, W. L. Chu and Y. C. Hu, Heterogenization of Heteropolyacids: A General Discussion on the Preparation of Supported Acid Catalysts, *Ind. Eng. Chem. Res.*, 1996, **35**(8), 2546–2560, DOI: **10.1021/ie950473s**.

53 W. L. Chu, X. G. Yang, X. K. Ye and Y. Wu, Adsorption of PMo12 and SiMo12 on Activated Carbon in Aqueous and Acidic Media, *Langmuir*, 1996, **12**(17), 4185–4189, DOI: **10.1021/la950412z**.

54 Y. Benseghir, A. Lemarchand, M. Duguet, P. Mialane, M. Gomez-Mingot, C. Roch-Marchal, T. Pino, M. H. Ha-Thi, M. Haouas, M. Fontecave, A. Dolbecq, C. Sassoye and C. Mellot-Draznieks, Co-Immobilization of a Rh Catalyst and a Keggin Polyoxometalate in the UiO-67 Zr-Based Metal-Organic Framework: In Depth Structural Characterization and Photocatalytic Properties for CO2 Reduction, *J. Am. Chem. Soc.*, 2020, **142**(20), 9428–9438, DOI: **10.1021/jacs.0c02425**.

55 K. M. Fahy, F. Sha, S. Reischauer, S. Lee, T.-Y. Tai and O. K. Farha, Role of Metal-Organic Framework Topology on Thermodynamics of Polyoxometalate Encapsulation, *ACS Appl. Mater. Interfaces*, 2024, **16**, 30296–30305, DOI: **10.1021/acsami.4c05016**.

56 G. Paille, M. Gomez-Mingot, C. Roch-Marchal, M. Haouas, Y. Benseghir, T. Pino, M. H. Ha-Thi, G. Landrot, P. Mialane, M. Fontecave, A. Dolbecq and C. Mellot-Draznieks, Thin Films of Fully Noble Metal-Free POM@MOF for Photocatalytic Water Oxidation, *ACS Appl. Mater. Interfaces*, 2019, **11**(51), 47837–47845, DOI: **10.1021/acsami.9b13121**.

57 M. Samaniyan, M. Mirzaei, R. Khajavian, H. Eshtiagh-Hosseini and C. Streb, Heterogeneous Catalysis by Polyoxometalates in Metal–Organic Frameworks, *ACS Catal.*, 2019, **9**(11), 10174–10191, DOI: **10.1021/acscatal.9b03439**.

58 I. Ullah, T. ul-Haq, A. A. Khan, A. Inayat, M. Shoaib, A. Haider, M. Saleem, S. M. Abbas, M. A. Pope and I. Hussain, Sodium Decavanadate Encapsulated Mn-BTC POM@MOF as High-Capacity Cathode Material for Aqueous Sodium-Ion Batteries, *J. Alloys Compd.*, 2023, **932**, 167647, DOI: **10.1016/j.jallcom.2022.167647**.

59 J. Wang, L. Li, Y. Liu, Z. Yuan, S. Meng, P. Ma, J. Wang and J. Niu, Intensifying Photocatalytic Baeyer-Villiger Oxidation of Ketones with the Introduction of Ru Metalloligands and Bimetallic Units in POM@MOF, *Inorg. Chem.*, 2024, **63**, 7325–7333, DOI: **10.1021/acs.inorgchem.4c00217**.

60 T.-T. Zhu, Z.-M. Zhang, W.-L. Chen, Z.-J. Liu and E.-B. Wang, Encapsulation of Tungstophosphoric Acid into Harmless MIL-101(Fe) for Effectively Removing Cationic Dye from Aqueous Solution, *RSC Adv.*, 2016, **6**(85), 81622–81630, DOI: **10.1039/c6ra16716k**.

61 Y. Ge, Y. Wang, G. Xu, Z. Fang, J. Bai and C. Li, Biomass Activated Carbon Supported Keggin-Type Polyoxometalate as an Electrode Material for High-Performance Acidic Aqueous Supercapacitors, *J. Electroanal. Chem.*, 2023, **947**, 117779, DOI: **10.1016/j.jelechem.2023.117779**.

62 J. Alcaniz-Monge, G. Trautwein, S. Parres-Esclapez and J. A. Macia-Agullo, Influence of Microporosity of Activated Carbons as a Support of Polyoxometalates, *Microporous Mesoporous Mater.*, 2008, **115**(3), 440–446, DOI: **10.1016/j.micromeso.2008.02.017**.

63 P. Palomino, J. Suarez-Guevara, M. Olivares-Marin, V. Ruiz, D. P. Dubal, P. Gomez-Romero, D. Tonti and E. Enciso, Influence of Texture in Hybrid Carbon-Phosphomolybdic Acid Materials on Their Performance as Electrodes in Supercapacitors, *Carbon*, 2017, **111**, 74–82, DOI: **10.1016/j.carbon.2016.09.054**.

64 M. Duguet, A. Lemarchand, Y. Benseghir, P. Mialane, M. Gomez-Mingot, C. Roch-Marchal, M. Haouas, M. Fontecave, C. Mellot-Draznieks, C. Sassoye and A. Dolbecq, Structure-Directing Role of Immobilized Polyoxometalates in the Synthesis of Porphyrinic Zr-Based Metal-Organic Frameworks, *Chem. Commun.*, 2020, **56**(70), 10143–10146, DOI: **10.1039/d0cc04283h**.

65 P. G. Vázquez, M. N. Blanco and C. V. Cáceres, Catalysts Based on Supported 12-Molybdophosphoric Acid, *Catal. Lett.*, 1999, **60**(4), 205–215, DOI: **10.1023/A:1019071410838**.

66 P. Villabrille, P. Vázquez, M. Blanco and C. Cáceres, Equilibrium Adsorption of Molybdosilicic Acid Solutions on Carbon and Silica:: Basic Studies for the Preparation of Ecofriendly Acidic Catalysts, *J. Colloid Interface Sci.*, 2002, **251**(1), 151–159, DOI: **10.1006/jcis.2002.8391**.

67 S.-M. Zhang, Y. Wang, Y.-Y. Ma, Z.-B. Li, J. Du and Z.-G. Han, Three-Dimensional Silver-Containing Polyoxotungstate Frameworks for Photocatalytic Aerobic Oxidation of Benzyl Alcohol, *Inorg. Chem.*, 2022, **61**, 20596–20607, DOI: **10.1021/acs.inorgchem.2c03472**.

68 W. Zhao, Y. Zhang, B. Ma, Y. Ding and W. Qiu, Oxidation of Alcohols with Hydrogen Peroxide in Water Catalyzed by Recyclable Keggin-Type Tungstoborate Catalyst, *Catal. Commun.*, 2010, **11**(6), 527–531, DOI: **10.1016/j.catcom.2009.12.010**.

69 W. Tian, Y. Hou, X. Wang, B. Lu, J. Zhao and Q. Cai, A Simple Polyoxometallate for Selective Oxidation of Benzyl Alcohol to Benzaldehyde with Hydrogen Peroxide, *Chin. J. Chem.*, 2012, **30**(2), 433–437, DOI: **10.1002/cjoc.201100144**.

70 B. L. Li, J. Li, X. M. Wang, Z. X. Wan and L. C. Wang, Phosphotungstic Acid Supported on Mesoporous Carbon as a Catalyst for the Oxidation of Benzyl Alcohol, *Kinet. Catal.*, 2013, **54**(1), 69–75, DOI: **10.1134/S0023158413010102**.

71 Y. Leng, J. Wang and P. Jiang, Amino-Containing Cross-Linked Ionic Copolymer-Anchored Heteropoly Acid for Solvent-Free Oxidation of Benzyl Alcohol with H_2O_2, *Catal. Commun.*, 2012, **27**, 101–104, DOI: **10.1016/j.catcom.2012.07.007**.

72 Y. Leng, J. Liu, P. Jiang and J. Wang, Heteropolyanion-Based Polymeric Hybrids: Highly Efficient and Recyclable Catalysts for Oxidation of Alcohols with H_2O_2, *RSC Adv.*, 2012, **2**(31), 11653–11656, DOI: **10.1039/c2ra22348a**.

73 X. Han, Y. Kuang, K. Ouyang, R. Kan, X. Tang, C.-T. Hung, L.-L. Liu, P.-H. Wu and S.-B. Liu, Role of Acidity over Rare Earth Metal Ion-Exchanged Heteropoly Tungstates during Oxidation of Alcohols, *J. Taiwan Inst. Chem. Eng.*, 2017, **70**, 23–31, DOI: **10.1016/j.jtice.2016.10.023**.

74 R. Chilivery, V. Chaitanya, J. Nayak, S. Seth and R. K. Rana, Heterogenization of Phosphotungstate Clusters into Magnetic Microspheres: Catalyst for Selective Oxidation of Alcohol in Water, *ACS Sustainable Chem. Eng.*, 2022, **10**(21), 6925–6933, DOI: **10.1021/acssuschemeng.1c07285**.

75 J. Diaz, L. R. Pizzio, G. Pecchi, C. H. Campos, L. Azocar, R. Briones, R. Romero, A. Henriquez, E. M. Gaigneaux and D. Contreras, Tetrabutyl Ammonium Salts of Keggin-Type Vanadium-Substituted Phosphomolybdates and Phosphotungstates for Selective Aerobic Catalytic Oxidation of Benzyl Alcohol, *Catalysts*, 2022, **12**(5), 507, DOI: **10.3390/catal12050507**.

76 X. Dong, D. Wang, K. Li, Y. Zhen, H. Hu and G. Xue, Vanadium-Substituted Heteropolyacids Immobilized on Amine-Functionalized Mesoporous MCM-41: A Recyclable Catalyst for Selective Oxidation of Alcohols with H_2O_2, *Mater. Res. Bull.*, 2014, **57**, 210–220, DOI: **10.1016/j.materresbull.2014.05.041**.

77 X. Dong, X. Zhang, P. Wu, Y. Zhang, B. Liu, H. Hu and G. Xue, Divanadium-Substituted Phosphotungstate Supported on Magnetic Mesoporous Silica Nanoparticles as Effective and Recyclable Catalysts for the Selective Oxidation of Alcohols, *ChemCatChem*, 2016, **8**(23), 3680–3687, DOI: **10.1002/cctc.201601077**.

78 D. R. Park, S. H. Song, U. G. Hong, J. G. Seo, J. C. Jung and I. K. Song, Redox Properties and Catalytic Oxidation Activities of Polyatom-Substituted $H_nPW_{11}M_1O_{40}$ (M = V, Nb, Ta, and W) Keggin Heteropolyacid Catalysts, *Catal. Lett.*, 2009, **132**(3–4), 363–369, DOI: **10.1007/s10562-009-0114-9**.

79 Y. Ding and W. Zhao, The Oxidation of Pyridine and Alcohol Using the Keggin-Type Lacunary Polytungstophosphate as a Temperature-Controlled Phase Transfer Catalyst, *J. Mol. Catal. A: Chem.*, 2011, **337**(1–2), 45–51, DOI: **10.1016/j.molcata.2011.01.012**.

80 D. Amitouche, M. Haouas, T. Mazari, S. Mouanni, R. Canioni, C. Rabia, E. Cadot and C. Marchal-Roch, The Primary Stages of Polyoxomolybdate Catalyzed Cyclohexanone Oxidation by Hydrogen Peroxide as Investigated by in Situ NMR. Substrate Activation and Evolution of the Working Catalyst, *Appl. Catal., A*, 2018, **561**, 104–116, DOI: **10.1016/j.apcata.2018.05.017**.

81 N. Mizuno and K. Kamata, Catalytic Oxidation of Hydrocarbons with Hydrogen Peroxide by Vanadium-Based Polyoxometalates, *Coord. Chem. Rev.*, 2011, **255**(19–20), 2358–2370, DOI: **10.1016/j.ccr.2011.01.041**.